Monthly Notices of the ROYAL ASTRONOMICAL SOCIETY

MNRAS **520,** L79–L84 (2023) https://doi.org/10.1093/mnrasl/slac155
Advance Access publication 2022 December 9

Effect of geometrically thin discs on precessing, thick flows: relevance to type-C QPOs

D. A. Bollimpalli [1,2,3★] P. C. Fragile [3,4★] and W. Kluźniak[2]

[1]*Max-Planck-Institut für Astrophysik, 85741 Garching b. München, Germany*
[2]*Nicolaus Copernicus Astronomical Center, ul. Bartycka 18, PL 00-716 Warsaw, Poland*
[3]*Department of Physics and Astronomy, College of Charleston, Charleston, SC 29424, USA*
[4]*Kavli Institute for Theoretical Physics, Kohn Hall, University of California, Santa Barbara, CA 93107, USA*

Accepted 2022 November 29. Received 2022 November 13; in original form 2022 October 6

ABSTRACT

Type-C quasi-periodic oscillations (QPOs) are the low-frequency QPOs most commonly observed during the hard spectral state of X-ray binary systems. The leading model for these QPOs is the Lense-Thirring precession of a hot geometrically thick accretion flow that is misaligned with respect to the black hole spin axis. However, none of the work done to date has accounted for the effects of a surrounding geometrically thin disc on this precession, as would be the case in the truncated disc picture of the hard state. To address this, we perform a set of general relativistic magnetohydrodynamics simulations of truncated discs misaligned with the spin axes of their central black holes. Our results confirm that the inner-hot flow still undergoes precession, though at a rate that is only 5 per cent of what is predicted for an isolated precessing torus. We find that the exchange of angular momentum between the outer thin and the inner thick disc causes this slow-down in the precession rate and discuss its relevance to type-C QPOs.

Key words: accretion, accretion discs – MHD – relativistic processes – methods: numerical – stars: black holes – X-rays: binaries.

1 INTRODUCTION

Many accreting black holes and neutron stars exhibit rapid variability in their X-ray light curves, which is often quasi-periodic in nature (indicated by broad peaks of power in the frequency domain). Further, they occasionally undergo outbursts during which the source transits through several different spectral states, as it simultaneously varies in luminosity and spectral hardness, tracing a 'q' shape in a hardness-intensity diagram, (Fender, Belloni & Gallo 2004; McClintock & Remillard 2006). The current best models that provide a framework for understanding these outbursts relate the changing spectra to a changing geometry of the accretion flow and the presence or absence of different physical components (e.g. a corona or jet) (Esin, McClintock & Narayan 1997; Begelman & Armitage 2014). The X-ray spectra observed in these systems are mainly composed of a soft, thermal component (below approximately 3 keV) and a hard power-law component (extending roughly between 10–100 keV). The soft component is thought to be due to thermal blackbody-like radiation from a relatively cold optically thick and geometrically thin disc. The non-thermal power-law component is thought to be generated from the inverse-Compton scattering of soft seed photons emitted from the disc by a radiatively inefficient cloud of hot electrons, often referred to as the 'corona.' The location and geometry of the corona are still under much debate, with some models placing it at the base of the jet (Martocchia & Matt 1996; Fabian et al. 2009; Parker et al. 2015), while others consider it to sandwich the disc (Galeev, Rosner & Vaiana 1979; Haardt & Maraschi 1993; Svensson 1996; Beloborodov 1999). The truncated-disc model envisions a third possible geometry with a standard-thin disc truncated well outside the last stable orbit, and the corona as a geometrically thick radiatively inefficient accretion flow filling in the inner gap (Eardley, Lightman & Shapiro 1975; Esin et al. 1997; Liu et al. 2007). Although all the above mentioned models can reproduce the observed X-ray spectra, the truncated disc model has the advantage of being able to simultaneously explain some of the observed variability properties. Irrespective of the model, a better understanding of the physical origins of the variability observed in each spectral state can serve as a powerful probe of the inner regions of accretion discs.

The nature of quasi-periodic oscillations (QPOs) varies from one spectral state to another. Broadly speaking, the QPOs observed in black hole systems are classified as high frequency ($\gtrsim$60 Hz) and low frequency ($\lesssim$30 Hz) (Remillard & McClintock 2006; Belloni 2010). Low-frequency QPOs are further classified into type-A, B, and C, of which the first two are observed in the intermediate states, during the transition from hard to soft spectral states (Motta 2016). Type-C QPOs are commonly observed in most accretion states (Motta et al. 2012; Motta 2016), although they are particularly prominent in the hard state. For these QPOs, both the fractional QPO amplitude and the phase-lag between the hard and soft photons measured at the QPO frequency are found to have an inclination dependence (Motta et al. 2015; van den Eijnden et al. 2017). Such a dependence strongly suggests a geometric origin for this QPO. For a detailed review of type-C QPOs, we refer the reader to Ingram & Motta (2019).

Most of the models invoked to explain type-C QPOs are based either on the geometry or the intrinsic properties of the disc. Possible mechanisms that have been invoked include trapped corrugation modes (*c*-modes) in the inner regions (Kato & Fukue 1980; Wagoner

★ E-mail: deepika@mpa-garching.mpg.de (DAB); fragilep@cofc.edu (PCF)

1999; Silbergleit, Wagoner & Ortega-Rodríguez 2001) or spiral density waves propagating back and forth between the disc inner radius and the Lindblad radius at some frequency (Tagger & Pellat 1999; Rodriguez et al. 2002). Along the same lines, oscillations of a standing shock in the accretion flow could also produce a type-C QPO; however, to produce the required frequencies, such a shock would need to be located quite far from the black hole (Chakrabarti & Titarchuk 1995). Another popular model is the relativistic precession model, which associates the type-C QPO with the nodal precession frequency of a geodesic particle orbit in relativity (Stella & Vietri 1998; Stella, Vietri & Morsink 1999).

A variation of this model, which seems to match observations of the type-C QPO particularly well, is, instead of having a particle or infinitesimal ring precess, have a finite inner region of the accretion flow precess (Ingram, Done & Fragile 2009). This model ties in with the truncated disc picture of the hard accretion state, in that, it is the hot thick flow inside the truncation radius (i.e. the corona) that is precessing (Ingram & Done 2011). This has the advantages of lowering the precession frequency into the proper range, naturally explaining the rise in the QPO frequency during the early phases of an outburst cycle (when the truncation radius is moving inward), and easily reproducing the inclination dependence seen in QPO observations (since precession is more apparent, the closer to the orbital plane one observes). This model also naturally explains the observed correlation between the QPO phase and the energy of the iron emission lines seen in phase-resolved spectroscopic studies (Ingram et al. 2016).

Previous numerical work involving magnetohydrodynamical simulations of *isolated* tilted thick discs have demonstrated global Lense-Thirring precession at frequencies matching observations (Fragile et al. 2007; Liska et al. 2018; White, Quataert & Blaes 2019). However, none of those studies consider the full truncated-disc geometry and especially the effects of the surrounding geometrically thin disc on the type-C QPO frequencies. The main concern for QPO models based on the Lense-Thirring precession of the hot thick flow is its coupling to the outer thin disc. Questions that need to be answered are: (1) How does the surrounding thin disc alter the precession, both in terms of its frequency and amplitude? (2) Will the coupling slow down the precession and eventually stop it, or perhaps boost the strength of the QPOs? The main objective of this paper is to address some of these questions.

For this purpose, we perform general relativistic magnetohydrodynamics (GRMHD) simulations of tilted truncated discs around rotating black holes. We evolve the simulations long enough to establish their steady-state behaviour which amounts to a significant fraction of the disc's precession period. The remainder of this paper is organized as follows: In Section 2, we describe the initial set-up of our simulations. In Section 3, we discuss the main result of our paper, that the outer thin disc slows down the precession of the inner thick disc. We conclude with a discussion in Section 4.

2 INITIAL SET-UP

2.1 Physical set-up

We performed three fully 3D GRMHD simulations of truncated accretion discs, all with the angular momentum axes of the disc and the black hole misaligned by an angle of $\beta_0 = 15^\circ$, as listed in Table 1; one is a high-resolution 4-level simulation (with dimensionless spin parameter $a_* = a/M = 0.9$), and two are 3-level low-resolution simulations with $a_* = 0.9$ and 0.5.

Table 1. Simulations presented in this paper.

Simulation	Spin (a_*)	Tilt (β_0)	Resolution	$t_{\rm end}$ [$r_{\rm g}/c$]
a9b15r15L4	0.9	15°	384x256x256	25 000
a9b15r15L3	0.9	15°	192x128x128	14 850
a5b15r15L3	0.5	15°	192x128x128	16 700

The initial set-up of all the simulations consists of a finite torus, surrounded by a thin disc. The torus is initialized following the procedure of Chakrabarti (1985) assuming a constant specific angular momentum, with its inner edge at $r_{\rm in} = 6.5\,r_{\rm g}$, pressure maximum at $r_{\rm cen} = 9\,r_{\rm g}$, and polytropic index of $\gamma = 5/3$, where $r_{\rm g} = GM/c^2$ is the gravitational radius. In all the simulations, a thin slab with fixed height, $H = 0.4r_{\rm g}$, surrounds the torus extending from $15r_{\rm g}$to the outer boundary of the simulations domain at $\approx 250r_{\rm g}$, with a density distribution

$$\rho(R, z) \propto \frac{\exp(-z^2/2H^2)}{\{1 + \exp[(15r_{\rm g} - R)/H]\}\{1 + \exp[(R - (40r_{\rm g})^{1.5})/H]\}}, \quad (1)$$

where $R = r\sin\theta$ is the cylindrical radius. The angular momentum in the thin disc is Keplerian. In order to maintain the desired thin structure, we use an artificial cooling function, as described in Fragile, Wilson & Rodriguez (2012a), but only applied to radii beyond $15r_{\rm g}$.

Both the torus and the slab are threaded with numerous small poloidal loops of magnetic field with alternating polarity, starting from a magnetic vector potential of the form

$$A_\phi \propto \frac{1}{1 + \exp(\delta)} \sqrt{P_{\rm g}} \sin(2\pi\, R/5H), \quad (2)$$

where $P_{\rm g}$ is the local gas pressure and $\delta = 10[(z/H)^2 + H^2/(R - r_{\rm ms})^2 + H^2/(40r_{\rm g}^{1.5} - R)^2 - 1]$, with $H = 0.6$ and $0.4r_{\rm g}$for the torus and thin disc regions, respectively, and $r_{\rm ms}$ is the location of the marginally stable orbit. The resulting magnetic field is normalized such that the ratio of the gas pressure to the magnetic pressure is initially $\geq$10 throughout the torus and thin disc. This field configuration prevents the accumulation of strong net flux in the inner regions, so we do not expect a magnetically arrested disc (MAD) to form. The background region surrounding the thin disc and torus is initialized with a non-magnetic gas with low density, $\rho = 10^{-5}\rho_{\rm max} r^{-1.5}$ and internal energy density, $e = 10^{-7} e_{\rm max} r^{-2.5}$, where $\rho_{\rm max}$ and $e_{\rm max}$ are the maximum gas density and internal energy density in the disc/torus.

2.2 Numerical set-up

All simulations are performed using *Cosmos++* (Anninos, Fragile & Salmonson 2005), with its five-stage strong-stability-preserving Runge–Kutta (SSPRK) time-stepping scheme (Spiteri & Ruuth 2002) and third-order piecewise-parabolic spatial reconstruction (Colella & Woodward 1984). The fluxes are calculated at zone interfaces using a two-wave HLL approximate Riemann solver (Harten, Lax & Leer 1983).

The simulations are performed in modified Kerr–Schild spherical-polar coordinates, which allow us to place the inner domain boundary inside the black hole event horizon. The grid is logarithmically spaced in r, extending over $r \in [1.4\,r_{\rm g},\ 40^{1.5}\,r_{\rm g}]$, and uniformly spaced in ϕ, covering the full $[0, 2\pi]$ domain. The polar angle θ is uniformly

spaced in the coordinate x_2, ranging from 0 to 1, with

$$\theta = \pi x_2 + \frac{1-h}{2}\sin(2\pi x_2), \tag{3}$$

where $h = 0.5$ is used to concentrate the grid cells close to the midplane (McKinney 2006). We cut out a small cone of opening angle $10^{-15}\pi$ near the poles to avoid calculating metric terms on the pole.

All simulations use a base resolution of 48 × 32 × 32 with an additional two or three levels of static mesh refinement added, with adjacent refinement levels differing in resolution by a factor of 2 in each dimension, to bring most of the grid up to a fiducial resolution of 192 × 128 × 128 or 384 × 256 × 256 for '3-level' and '4-level' simulations, respectively. The initial two levels of refinement are used to resolve both the torus and the thin slab, which is common for both the 3-level and 4-level simulations. The torus region is refined with two refinement levels in the regions within $1.4 < r/r_g < 24$ and $0.14\pi < \theta < 0.86\pi$, and $1.4 < r/r_g < 21$ and $0.2\pi < \theta < 0.8\pi$, respectively. The thin disc region within $12.6 < r/r_g < 253$ and $0.4\pi < \theta < 0.6\pi$ is refined twice. For the 4-level simulation, an additional refinement layer is used to better resolve the thin disc over $r \in [10.5\,r_g, 60\,r_g]$.

Outflow boundary conditions are used at both the inner and the outer radial boundaries. We use pole-axis boundary conditions near the poles, where information from the corresponding zone across the pole is used for calculating gradients, although fluxes, magnetic fields, and electric fields (emf's) are zeroed out on the faces and edges that touch the pole. Lastly, periodic boundary conditions are implemented along the azimuthal direction. The zero-divergence of the magnetic fields is ensured using a constrained transport scheme (Fragile, Wilson & Rodriguez 2012b).

As expected, once the simulations are set to evolve, the initial magnetic fields trigger the magnetorotational instability, causing turbulence to transport the angular momentum and thus allow accretion. The heat generated in this process inflates the torus, thus forming a hot thick flow in the inner regions. The cooling function, which is set to work in the outer thin slab region ($r \geq 15r_g$), acts as a heat sink and helps to maintain the target thickness, $H/r \approx 0.05$. The simulations have been run for more than $25\,000 r_g/c$ for the 4-level simulation and around $15\,000 r_g/c$ for the 3-level simulations. All of them have successfully maintained a two-component flow, as anticipated.

3 RESULTS

3.1 Precession angle

We compute the precession angle, γ, by adopting the same formalism as in Fragile et al. (2007); this angle quantifies how much the disc angular momentum vector has twisted, or precessed, around the black hole spin axis, as

$$\gamma(r) = \cos^{-1}\left[\frac{\boldsymbol{J}_{\rm BH}\times\boldsymbol{J}_{\rm disc}(r)}{|\boldsymbol{J}_{\rm BH}\times\boldsymbol{J}_{\rm disc}(r)|}\cdot\hat{\mathbf{y}}\right], \tag{4}$$

where $\boldsymbol{J}_{\rm BH} = (-aM\sin\beta_0\hat{x},\ 0,\ aM\cos\beta_0\hat{z})$ is the angular momentum vector of the black hole, and

$$(J_{\rm disc})_\eta\,(r) = \frac{\epsilon_{\mu\nu\sigma\eta}L^{\mu\nu}S^\sigma}{2\sqrt{-S^\alpha S_\alpha}} \tag{5}$$

for $\eta = 1, 2, 3$ corresponds to the Cartesian vector components of the angular momentum vector of the disc as measured in asymptotically flat space. Here

$$L^{\mu\nu} = \int \left(x^\mu T^{\nu 0} - x^\nu T^{\mu 0}\right) {\rm d}^3x \tag{6}$$

and $S^\sigma = \int T^{\sigma 0}{\rm d}^3x$, where $T^{\mu\nu}$ is the MHD stress-energy tensor of the fluid [see Appendix A]. As a reminder, the angular momentum vector of the disc at $t = 0$ is aligned along the direction of the $\hat{\mathbf{z}}$ unit vector. To avoid the degeneracy in cosine for angles greater than 180°, we also look at the projection of $\boldsymbol{J}_{\rm BH}\times\boldsymbol{J}_{\rm disc}(r)$ onto $\hat{\mathbf{x}}$.

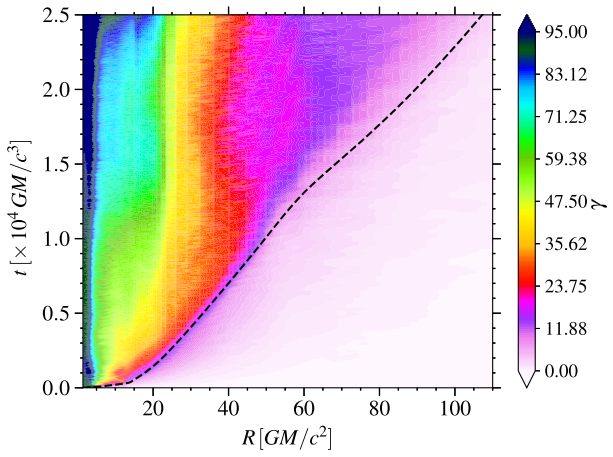

Figure 1. Space-time plot of the precession angle, γ (measured in degrees) for simulation a9b15r15L4. The dashed curve represents the bending wave propagating at half the sound speed. The consistent precession angle seen between 5 and 20 r_g at any given time suggest that this region is undergoing rigid-body precession.

Fig. 1 shows the evolution of the precession angle for simulation a9b15r15L4. There is a clear signature of a precession front starting from the inner thick-disc region, which propagates to the outer radii (from lower left to upper right) over time. The propagation happens on the bending wave time-scale shown by the black–dashed curve.[1] Radii very close to the black hole undergo rapid precession to angles up to 90°, holding there for a period until the surrounding regions begin to catch up. Beyond $20r_g$, the initial precession is much more modest ($\gamma \lesssim 30°$). This value also freezes in after a very short period of time ($<2000r_g/c$ after the bending wave passes); this frozen-in twist is noted by the vertical stripes of colour in Fig. 1, such as the vertical red patch at $\approx 40r_g$. Inside of $20r_g$, however, the behaviour is much different. Rather than vertical stripes of constant colour, we see nearly simultaneous variation of colour between 5 and $20r_g$. This simultaneous variation indicates *solid-body precession*; all radii are experiencing the same degree of precession at roughly the same time. An example is the nearly horizontal dark green band around a time of $10^4 r_g/c$, indicating that the inner torus has precessed ≈60° by this time.

3.2 Effect of the outer thin disc on the precessing inner thick disc

The Lense-Thirring precession frequency of a test particle in an orbit misaligned with the spin-axis of the black hole is given by

$$\Omega_{\rm LT} = \Omega_\phi\left[1 - \sqrt{1 - \frac{4a_*}{r^{3/2}} + \frac{3a_*^2}{r^2}}\right]. \tag{7}$$

[1] Bending waves propagate at roughly half the sound speed, c_s, so the dashed curve is given by $\int 2{\rm d}r/\langle c_s(r,t)\rangle_{\theta,\phi}$.

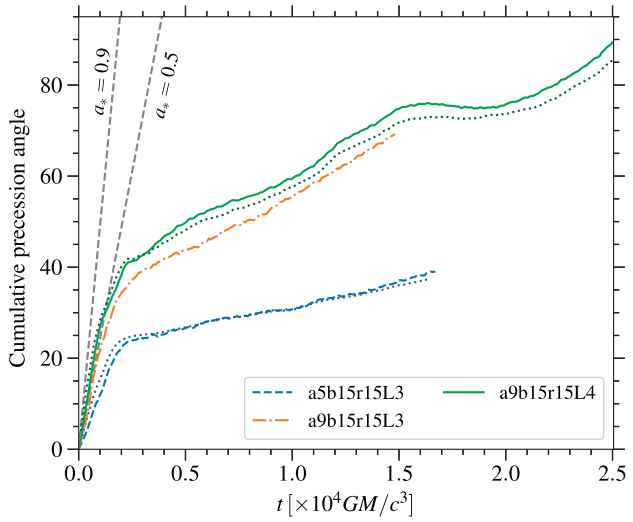

Figure 2. Time evolution of the cumulative precession angle over the range 5–15r_g. The slopes of these curves give the precession rates. The grey–dashed lines represent the precession rates estimated from equation (8). The coloured–dotted curves represent the precession estimated using equation (A4) for the simulations a9b15r15L4 and a5b15r15L3.

For an isolated torus-like structure between an inner and outer radius, r_i and r_o, precessing as a solid body, the angular frequency of precession is computed from weighting Ω_{LT} by the angular momentum of the torus:

$$\Omega_{prec} = \frac{\int_{r_i}^{r_o} \Omega_{LT} \Sigma r^3 \Omega_\phi \mathrm{d}r}{\int_{r_i}^{r_o} \Sigma r^3 \Omega_\phi \mathrm{d}r}, \tag{8}$$

where $\Omega_\phi(r)$ is the local angular velocity. Assuming a power-law profile for the surface density, $\Sigma(r) \sim \Sigma(r_i)(r/r_i)^{-\zeta}$, one can arrive at an analytical estimate of Ω_{prec} given by equation (43) in Fragile et al. (2007).

Fig. 2 shows the cumulative precession angle for matter between 5 and 15r_g in our three simulations. We exclude the region inside $r = 5r_g$, because tilted discs have effective inner radii well outside of the marginally stable limit (Fragile 2009). The expected precession rates (equation 8) for tori extending over this range of radii are represented by the grey–dashed lines, with $\zeta = -6.1$ for the $a_* = 0.9$ simulation and -5.2 for the $a_* = 0.5$ one. We see that the predicted precession rates agree reasonably well with the early ($t \lesssim 1000\ r_g/c$) behavior of the simulations. However, after $t \approx 2000 r_g/c$, which is roughly when the bending wave reaches the transition region ($15 \lesssim r \lesssim 20r_g$, see Fig. 1), the slopes of the cumulative precession curves change dramatically. The precession rate decreases by more than 95 per cent to a rate comparable to what equation (8) would give if r_o were $40r_g$. This establishes the key results of our paper: *the outer thin disc clearly affects the precession of the inner thick disc by reducing its rate*. It is encouraging that we find nearly identical precession rates in the low- and high-resolution $a_* = 0.9$ simulations, suggesting that this conclusion is robust. To ensure that the decrease in the precession rate is due to the outer thin disc, we performed another simulation identical to a9b15r15L4, except that the outer thin disc is absent, and found that it precesses continuously at the rate predicted by equation (8).

The decrease in the precession rate in the truncated disc simulations can be attributed to the exchange of angular momentum between the thick and thin discs. We discuss how to estimate this effect in Appendix A. In particular, if we include both the torque and flux terms in equation (A4), then we find remarkable agreement between equation (A1) and the simulation results, as shown by the dotted curves in Fig. 2. It is worth pointing out that if we exclude the flux terms in equation (A4), we recover the expected precession rates from equation (8).

4 DISCUSSION

Over the last decade, the Lense-Thirring precession model by Ingram et al. (2009) has gained wide popularity for explaining the type-C QPOs observed in X-ray binary systems. The dependence of the precession frequency on the outer radius of the torus in this model, facilitates an independent measurement of the truncation radius when compared to observations. According to Ingram et al. (2009), the estimated frequencies for an isolated torus with r_i between 5–10r_g and r_o varying from 10–50r_g can produce frequencies in the observed range of 0.01–10 Hz. However, as we showed in the previous section, the presence of a thin disc outside the hot thick flow decreases the precession frequency by about 95 per cent. This has direct implications for the truncation radius estimation.

For a typical black hole mass of 10 $M_\odot$, the precession frequencies resulting from our simulations are roughly 0.14 and 0.05 Hz for $a_* = 0.9$ and 0.5, respectively. These frequencies fall near the lower end of the type-C QPO range (Remillard & McClintock 2006). To reach the upper end of the frequency range requires decreasing the size of the precessing torus. In this way, the slower precession frequencies noted in this work actually help relieve some of the tensions between the Lense-Thirring precession model and some type-C QPO observations. One such example is the 2.2 Hz QPO observed in the black hole binary system GRS 1915+105 (Nathan et al. 2022). According to equation (8), the outer edge of an isolated torus precessing around a 10.1 $M_\odot$ black hole with $a_* = 0.998$ would need to be around $41r_g$ to produce a frequency this low. However, the inferred truncation radius from phase-resolved spectroscopy of this particular QPO is $1.43^{+0.01}_{-0.02} r_g$ (Nathan et al. 2022). One way this conflict could be resolved is if the outer thin disc decreases the Lense-Thirring precession frequency of the inner torus as found in our work. Assuming that the percentage decrease in the precession frequency does not vary with the truncation radius, we can match the 2.2 Hz frequency with an outer edge now only at $\approx 11r_g$. This is still in conflict with the phase-resolved spectroscopy results, but moves things considerably in the right direction. Of course, we do not know yet how the precession rate will vary as the truncation radius changes, something that will need to be explored in future studies. It is worth noting that although a smaller precessing region may help match the observational data, it possibly exacerbates the long-standing question about how that region emits enough luminosity to dominate the timing signal. Lastly, Liska et al. (2021) reported that for extreme tilt angles (45–60°), geometrically thin discs could fragment into sub-discs each precessing at different rates. It would be interesting to test our model for such extreme tilt angles to study the possibility of disc tearing in the outer, thin disc and how it affects the precession rate

We conclude that in a truncated-disc geometry, the rate of Lense-Thirring precession of the hot thick flow around a black hole can be significantly reduced from the isolated case by the advected angular momentum fluxes from the surrounding thin disc. In principle, this result could potentially be relevant to other astrophysical phenomena based on Lense-Thirring precession, such as tilted discs in tidal disruption events, where the exchange of angular momentum between the incoming debris stream from the disrupted star and the precessing disc around the supermassive black hole could potentially slow down

the precession or even halt it if the fluxes are strong enough; this is something that will be studied with future simulations.

ACKNOWLEDGEMENTS

We want to thank Pavel Ivanov for helpful discussions regarding this work. This research was partly supported by the Polish Narodowe Centrum Nauki (NCN) grants 2018/29/N/ST9/02139, 2019/33/B/ST9/01564 and Polish National Agency for Academic Exchange grant PPN/IWA/2018/1/00099/U/0001. Simulations in this work were performed using the Cyfronet Prometheus cluster, part of the PL-Grid computing network and the Max Planck Computing & Data Facility. This work also used the Extreme Science and Engineering Discovery Environment (XSEDE), which is supported by National Science Foundation grant (NSF) number ACI-1548562. PCF gratefully acknowledges the support of the NSF through grants AST1616185, PHY-1748958, and AST-1907850. This work was performed in part at the Aspen Center for Physics, which is supported by NSF grant PHY-1607611.

DATA AVAILABILITY

The data underlying this paper will be shared upon reasonable request to the corresponding author.

REFERENCES

Anninos P., Fragile P. C., Salmonson J. D., 2005, ApJ, 635, 723
Begelman M. C., Armitage P. J., 2014, ApJ, 782, L18
Belloni T. M., 2010, in Belloni T., ed., Vol. 794, Lecture Notes in Physics, Vol. 794, States and Transitions in Black Hole Binaries. Springer-Verlag, Berlin, p. 53
Beloborodov A. M., 1999, ApJ, 510, L123
Chakrabarti S. K., 1985, ApJ, 288, 1
Chakrabarti S., Titarchuk L. G., 1995, ApJ, 455, 623
Colella P., Woodward P. R., 1984, J. Comput. Phys., 54, 174
Eardley D. M., Lightman A. P., Shapiro S. L., 1975, ApJ, 199, L153
Esin A. A., McClintock J. E., Narayan R., 1997, ApJ, 489, 865
Fabian A. C. et al., 2009, Nature, 459, 540
Fender R. P., Belloni T. M., Gallo E., 2004, MNRAS, 355, 1105
Fragile P. C., 2009, ApJ, 706, L246
Fragile P. C., Blaes O. M., Anninos P., Salmonson J. D., 2007, ApJ, 668, 417
Fragile P. C., Wilson J., Rodriguez M., 2012a, MNRAS, 424, 524
Fragile P. C., Wilson J., Rodriguez M., 2012b, MNRAS, 424, 524
Galeev A. A., Rosner R., Vaiana G. S., 1979, ApJ, 229, 318
Haardt F., Maraschi L., 1993, ApJ, 413, 507
Harten A., Lax P. D., Leer B. V., 1983, SIAM Rev., 25, 35
Ingram A. R., Motta S. E., 2019, New A Rev., 85, 101524
Ingram A., Done C., 2011, MNRAS, 415, 2323
Ingram A., Done C., Fragile P. C., 2009, MNRAS, 397, L101
Ingram A., van der Klis M., Middleton M., Done C., Altamirano D., Heil L., Uttley P., Axelsson M., 2016, MNRAS, 461, 1967
Kato S., Fukue J., 1980, PASJ, 32, 377
Liska M., Hesp C., Tchekhovskoy A., Ingram A., van der Klis M., Markoff S. B., Van Moer M., 2021, MNRAS, 507, 983
Liska M., Hesp C., Tchekhovskoy A., Ingram A., van der Klis M., Markoff S., 2018, MNRAS, 474, L81
Liu B. F., Taam R. E., Meyer-Hofmeister E., Meyer F., 2007, ApJ, 671, 695
Martocchia A., Matt G., 1996, MNRAS, 282, L53
McClintock J. E., Remillard R. A., 2006, in Lewin W., van der Klis M., eds, Camb. Astrophys. Ser. No. 39, Vol. 39, Compact stellar X-ray sources. Cambrdige Univ. Press, Cambridge, p. 157
McKinney J. C., 2006, MNRAS, 368, 1561
Motta S. E., 2016, Astron. Nachr., 337, 398
Motta S. E., Casella P., Henze M., Muñoz-Darias T., Sanna A., Fender R., Belloni T., 2015, MNRAS, 447, 2059
Motta S., Homan J., Muñoz Darias T., Casella P., Belloni T. M., Hiemstra B., Méndez M., 2012, MNRAS, 427, 595
Nathan E. et al., 2022, MNRAS, 511, 255
Parker M. L. et al., 2015, ApJ, 808, 9
Pringle J. E., 1992, MNRAS, 258, 811
Remillard R. A., McClintock J. E., 2006, ARA&A, 44, 49
Rodriguez J., Varnière P., Tagger M., Durouchoux P., 2002, A&A, 387, 487
Silbergleit A. S., Wagoner R. V., Ortega-Rodríguez M., 2001, ApJ, 548, 335
Spiteri R. J., Ruuth S. J., 2002, SIAM J. Numer. Anal., 40, 469
Stella L., Vietri M., 1998, ApJ, 492, L59
Stella L., Vietri M., Morsink S. M., 1999, ApJ, 524, L63
Svensson R., 1996, A&AS, 120, 475
Tagger M., Pellat R., 1999, A&A, 349, 1003
van den Eijnden J., Ingram A., Uttley P., Motta S. E., Belloni T. M., Gardenier D. W., 2017, MNRAS, 464, 2643
Wagoner R. V., 1999, Phys. Rep., 311, 259
White C. J., Quataert E., Blaes O., 2019, ApJ, 878, 51
Zhuravlev V. V., Zhuravlev P. B., Fragile P. C., Morales Teixeira D., 2014, ApJ, 796, 104

APPENDIX A: CALCULATION OF PRECESSION RATE

Let J_1 and J_2 be orthogonal vector components of the angular momentum of the precessing torus projected onto the equatorial plane of the black hole. We can then define the precession angle, γ, of the torus extending from r_i to r_o as $\tan\gamma = J_2/J_1$. Differentiating with respect to time gives us the precession rate (Zhuravlev et al. 2014),

$$\frac{\partial\gamma}{\partial t} = \frac{1}{J_1^2 + J_2^2}\left(J_1\frac{\partial J_2}{\partial t} - J_2\frac{\partial J_1}{\partial t}\right). \tag{A1}$$

All we need to do is compute the terms J_i and $\partial J_i/\partial t$ (for $i = 1, 2$) from the simulation data.

For J_i, we take

$$J_i = \int_{r_\mathrm{i}}^{r_\mathrm{o}} \mathrm{d}r\mathrm{d}\theta\mathrm{d}\phi\sqrt{-g}l_i, \tag{A2}$$

where $l_1 = l^x\cos\beta_0 + l^z\sin\beta_0$ and $l_2 = l^y$; the vector components of the angular momentum density ($\boldsymbol{l}$) in Cartesian coordinates are $l^x = yT^{tz} - zT^{ty}$, $l^y = zT^{tx} - xT^{tz}$, and $l^z = xT^{ty} - yT^{tx}$; and $T^{\mu\nu} = (\rho h + 2P_\mathrm{m})u^\mu u^\nu + (P_\mathrm{g} + P_\mathrm{m})g^{\mu\nu} - b^\mu b^\nu$ is the stress-energy tensor of the fluid in the MHD limit, where $h = 1 + \epsilon + P_\mathrm{g}/\rho$ is the specific enthalpy, ϵ is the specific internal energy density, P_m is the magnetic pressure, u^μ is the fluid four-velocity, and b^μ is the four-vector magnetic field measured by an observer comoving with the fluid.

To predict the time-derivatives of the angular momentum in a simple model, we use the angular momentum conservation equation (Pringle 1992)

$$\frac{\partial\boldsymbol{L}}{\partial t} + \frac{1}{r}\frac{\partial}{\partial r}\left(rV^r\boldsymbol{L}\right) = \boldsymbol{\Omega}_\mathrm{LT}\times\boldsymbol{L}, \tag{A3}$$

where $\boldsymbol{L}$ is the angular momentum vector per unit surface area and V^r is the radial velocity. Technically, this equation was derived in the diffusive regime, but as we show, it works well even for our truncated discs. We have ignored the viscous terms in the above conservation equation, as we find them to be negligible when compared to the Lense-Thirring torque and angular momentum

fluxes in our simulations. Integrating the vector components of the above equation over the surface area, we get

$$\frac{\partial J_i}{\partial t} = \mp \int_{r_\mathrm{i}}^{r_\mathrm{o}} \mathrm{d}r\mathrm{d}\theta\mathrm{d}\phi\sqrt{-g}\Omega_{\mathrm{LT}} l_j - \left[F_i|_{r_\mathrm{o}} - F_i|_{r_\mathrm{i}}\right], \tag{A4}$$

where the minus sign and $j = 2$ are taken for $i = 1$, and the plus sign and $j = 1$ are taken for $i = 2$. The first term on the right-hand-side is the usual Lense-Thirring torque term, and the terms within braces represent the angular momentum flux through the boundaries, r_i and r_o, given by

$$F_i = \int \mathrm{d}\theta\mathrm{d}\phi\sqrt{-g} l_i V^r. \tag{A5}$$

This paper has been typeset from a TEX/LATEX file prepared by the author.